Physics in Medicine & Biology

IPEM Institute of Physics and Engineering in Medicine

ACCEPTED MANUSCRIPT

Reducing 4DCBCT imaging dose and time: exploring the limits of adaptive acquisition and motion compensated reconstruction

To cite this article before publication: Benjamin King Fung Lau *et al* 2022 *Phys. Med. Biol.* in press https://doi.org/10.1088/1361-6560/ac55a4

Reducing 4DCBCT Imaging Dose and Time: Exploring the Limits of Adaptive Acquisition and Motion Compensated Reconstruction

Benjamin K.F. Lau [1], Tess Reynolds [1], Paul J. Keall [1], Jan-Jakob Sonke [2], Shalini K. Vinod [3 4], Owen Dillon [1] and Ricky T. O'Brien [1]

[1] ACRF Image X Institute, The University of Sydney, New South Wales, Australia.

[2] Department of Radiation Oncology, The Netherlands Cancer Institute, Amsterdam, The Netherlands.

[3] Liverpool & Macarthur Cancer Therapy Centres, Liverpool Hospital, Liverpool, New South Wales, Australia.

[4] South Western Sydney Clinical School, The University of New South Wales & Ingham Institute for Applied Medical Research, Liverpool, New South Wales, Australia.

Abstract

This study investigates the dose and time limits of adaptive 4DCBCT acquisitions (adaptive-acquisition) compared with current conventional 4DCBCT acquisition (conventional-acquisition). We investigate adaptive-acquisitions as low as 60 projections (~25 second scan, 6 projections per respiratory phase) in conjunction with emerging image reconstruction methods.

4DCBCT images from 20 patients recruited into the ADaptive CT Acquisition for Personalized Thoracic Imaging (ADAPT) clinical study (NCT04070586) were resampled to simulate faster and lower imaging dose acquisitions.

All acquisitions were reconstructed using Feldkamp-Davis-Kress (FDK), McKinnon-Bates (MKB), Motion Compensated FDK (MCFDK), Motion Compensated MKB (MCMKB) and Simultaneous Motion Estimation and Image Reconstruction (SMEIR) algorithms. All reconstructions were compared against conventional-acquisition 4DFDK-reconstruction using Structural SIMilarity Index (SSIM), Signal-to-Noise Ratio (SNR), Contrast-to-Noise-Ratio (CNR), Tissue Interface Sharpness Diaphragm (TIS-D), Tissue Interface Sharpness Tumor (TIS-T) and Center of Mass Trajectory (COMT) for difference in diaphragm and tumor motion.

All reconstruction methods using 110-projection adaptive-acquisition (11 projections per respiratory phase) had a SSIM of greater than 0.92 relative to conventional-acquisition 4DFDK-reconstruction. Relative to conventional-acquisition 4DFDK-reconstruction, 110-projection adaptive-acquisition MCFDK-reconstructions images had 60% higher SNR, 10% higher CNR, 30% higher TIS-T and 45% higher TIS-D on average. The 110-projection adaptive-acquisition SMEIR-reconstruction images had 123% higher SNR, 90% higher CNR, 96% higher TIS-T and 60% higher TIS-D on average. The difference in diaphragm and tumor motion compared to conventional-acquisition 4DFDK-reconstruction was within submillimeter accuracy for all acquisition reconstruction methods.

Adaptive-acquisitions resulted in faster scans with lower imaging dose and equivalent or improved image quality compared to conventional-acquisition. Adaptive-acquisition with motion compensated-reconstruction enabled scans with as low as 110 projections to deliver acceptable image quality. This translates into 92% lower imaging dose and 80% less scan time than conventional-acquisition.

1. Introduction

Four-dimensional cone beam computed tomography (4DCBCT) is frequently implemented in lung cancer radiation therapy for image guidance and patient positioning [1]. This study defines conventional-acquisition as a 1,320 projection 240 second 4DCBCT acquisition (projections retrospectively sorted by respiratory phase). Currently, widespread implementation of conventional-acquisition has been hindered due to higher doses (1,320 projections), long scan times (240 seconds) and variable but low image quality [2-5]. Hence, it is of interest to formulate methods that can acquire images with far fewer projections within a shorter timeframe while maintaining image quality compared to the current clinical standard.

Previous studies have proposed several methods to reduce imaging dose and scan time, while maintaining or improving image quality. Potential solutions include gantry speed variation [2, 3, 5], novel image reconstruction algorithms [2, 3, 6-9], and image acquisition adaptation in response to real-time patient breathing rate [9-17].

This study aims to reduce scan time and imaging time as low as possible (with image quality comparable to conventional-acquisition 4DFDK-reconstruction) by examining novel image reconstruction techniques and adaptive image acquisition in response to real-time breathing, referred to as adaptive 4DCBCT (referred in some literature as respiratory motion guided 4DCBCT or RMG-4DCBCT). [18]. In this paper adaptive 4DCBCT is defined as adaptive-acquisition. Adaptive-acquisition attempts to achieve even angular spacing between projections at each respiratory phase through real-time modulation of kV acquisition rate and gantry rotational speed in response to real-time changes in the patient's breathing rate [9, 12, 14, 19]. The adaptive-acquisition protocol has been clinically implemented for lung cancer radiotherapy patients in the Adaptive CT acquisition for Personalized Thoracic Imaging (ADAPT) trial (NCT04070586).

Recent literature has proposed and demonstrated that combining adaptive-acquisitions with motion compensated reconstruction algorithms can reduce imaging dose up to 85% and scan times by up to 75%

whilst maintaining or improving image quality compared to current clinical standard [9, 18, 20]. However, no study has investigated reducing dose and scan time as much as possible within the limitations of reconstruction algorithms by combining adaptive-acquisition data with emerging image reconstruction methods, particularly iterative methods. Addressing this gap in knowledge is the focus of this work.

This study evaluates adaptive-acquisition and resampled adaptive-acquisition, compared with conventional-acquisitions, reconstructed with emerging reconstruction methods using data from the ADAPT clinical trial. The study will determine the projection adaptive-acquisition and reconstruction protocol that can provide acceptable image quality in a clinically viable time frame, while minimizing scan time and imaging dose.

2. Method

The focus of this study was to resample adaptive-acquisition scans to simulate faster and lower image dose scans. To perform this, adaptive-acquisition and conventional-acquisition scans were obtained as part of the ADAPT clinical trial for lung cancer radiotherapy. The acquisition, resampling, image reconstruction, and evaluation workflow is outlined in Figure 1, where Figure 2 details the resampling process. Table 1 shows the mathematical summary of the reconstruction algorithms evaluated in this study. Table 2 details the mathematical summary of the image quality metrics used.

ADAPT Clinical Trial Overview

Ethical, regulatory, and legal compliance for the ADAPT clinical trial were obtained (ethics approval 2019/ETH09968, clinical trial registry number NCT04070586).

4DCBCT images from 20 lung cancer radiotherapy patients enrolled into the ADAPT trial were analyzed in this study. An Elekta Synergy linear accelerator (Elekta AB, Sweden) was employed to provide acquisition and treatment. Elekta Synergy utilizes fixed kV/mA per projection, it was tuned to acquire patient scans at 120kV, 20mA and 25ms (0.5mAs per projection). 4DCBCT scans were acquired on two separate days of treatment. The ADAPT patient dataset consisted of a planning 4DCT, conventional-acquisition, 200-projection adaptive-acquisition scan and a 600-projection adaptive-acquisition scan. The patient cohort had a conventional-acquisition for alignment and received radiotherapy treatment in accordance with routine standard of care. The 200-projection and 600-projection adaptive-acquisition scans were acquired immediately after patient treatment.

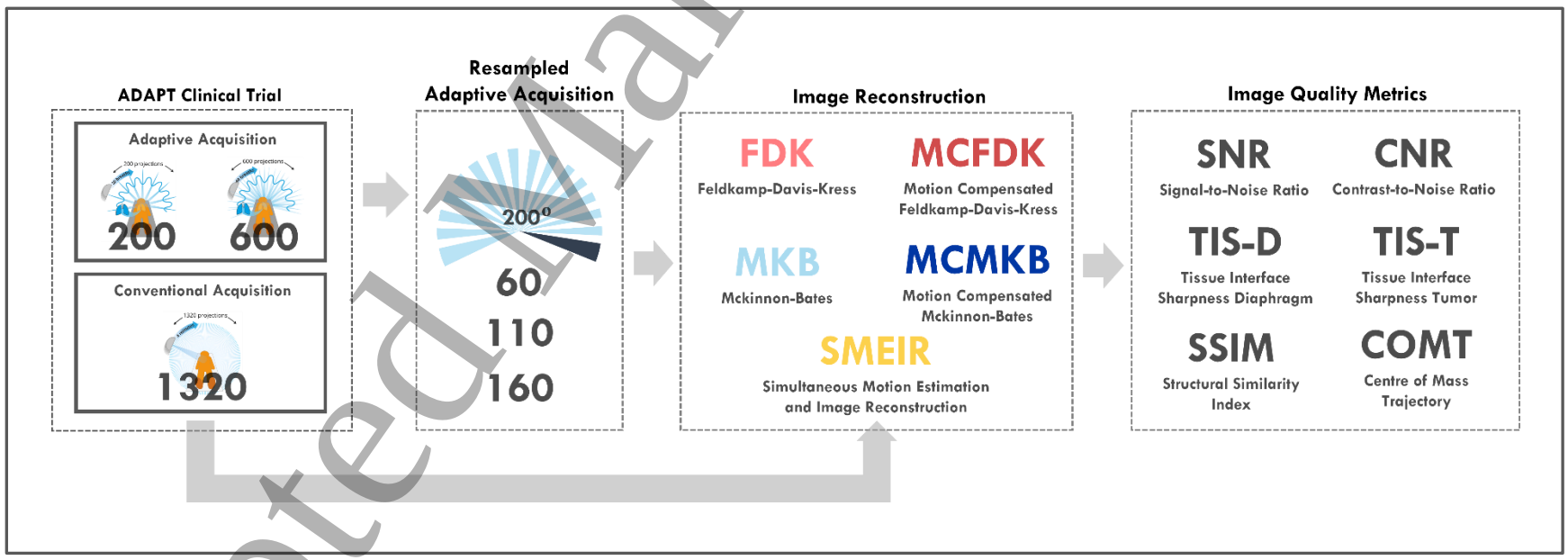

Figure 1: Study design schematic. Projections were acquired using adaptive- and conventional-acquisition methods. To simulate faster and lower dose scans, 200-projection adaptive-acquisitions were resampled into 60- and 110-projection acquisitions and 600-projection adaptive-acquisitions were resampled into 160-projection acquisitions. All acquisitions were reconstructed with 5 different image reconstruction algorithms. Reconstructions were evaluated using image quality metrics, using 1320-projection conventional-acquisition 4DFDK-reconstruction as the baseline.

Conventional- and Adaptive-Acquisition

Current clinical standard conventional-acquisition rotates the gantry 200° over 4 minutes with a constant 5.5 Hz acquisition rate. For adaptive-acquisition, the gantry rotation speed and acquisition rate are modulated to ensure even angular separation between projections at each patient respiratory phase. Further information on the ADAPT trial's adaptive-acquisition protocol has been detailed in [18] and [10].

Faster and lower dose adaptive-acquisitions were simulated by resampling 200- and 600-projection adaptive-acquisition by 25% or 50%. Initially the adaptive-acquisitions were resampled by removing respiratory phase projections according to the resampling rate (i.e. 200-projections were halved into 100-projections by skipping every second breathing cycle frame) whilst maintaining even angular spacing. The resampled adaptive-acquisitions were also inclusive of 10 additional projections at the end of the arc to ensure a 200° projection arc was maintained for comparison against 200° arc conventional- and adaptive-acquisitions. The 200-projection adaptive-acquisition scan was resampled to 60- and 110-projection scans, whilst the 600-projection adaptive-acquisition scan was resampled to 160-projection scans.

The resampling approach was not applied to the conventional 1320-projection acquisitions as the study focused on what would happen when adaptive acquisitions acquired less projections. If the same resampling approach was applied to conventional 1320-projection acquisitions, it may skew certain respiratory phases as this acquisition method does not ensure all phases are evenly sampled.

The schematic for this resampling process is shown in Figure 2.

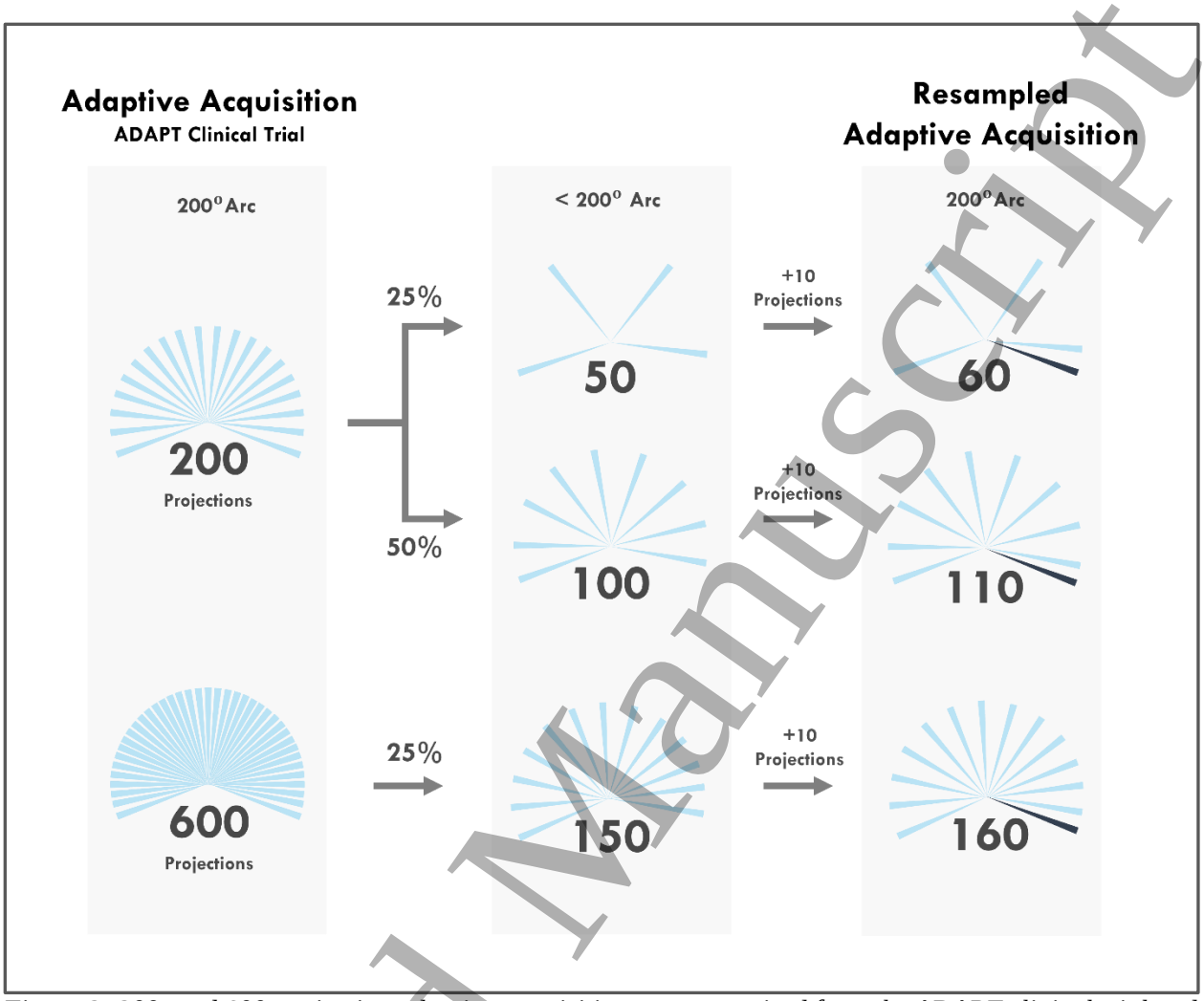

Figure 2: 200- and 600-projection adaptive-acquisitions were acquired from the ADAPT clinical trial and simulated into faster and lower dose acquisitions. 200- and 600-projection adaptive-acquisitions were resampled into 25% and 50% projection acquisitions initially. 10 projections (depicted by the dark blue projections) at the end of the arc were included for each resampled acquisition to maintain a 200° projection arc. As a result, 60-, 110- and 160-projection adaptive-acquisitions were simulated.

Imaging Dose

Imaging dose for adaptive-acquisitions were assumed to be linear to the projection count i.e. reduction from 1,320-projection conventional-acquisition (7.2 mSv, as noted in the medical physicist dose report) to a 110-projection adaptive-acquisition (approximately 0.6 mSv) equates to a 92% dose reduction.

Imaging Time

We acquire 1 projection per respiratory bin (in our case 10) per breath i.e. the 200 and 600 projection scans last 20 and 60 patient breaths respectively. The resampled acquisitions would perform the same i.e. the 60 projection scan would take 6 breaths.

Therefore, acquisition time for resampled adaptive-acquisitions were estimated based on projection number. 200- and 600-projection adaptive-acquisitions were acquired from the ADAPT clinical trial, the acquisition time stated in Table 3 were averaged across 2 fractions. 60- and 110-projection adaptive-acquisition times were estimated from 200-projection adaptive-acquisitions. 160-projection adaptive-acquisition times were estimated from 600-projection adaptive-acquisitions.

Image Reconstruction Hardware and Settings

The implementation of reconstruction algorithms was performed using the Reconstruction Tool Kit (RTK) [21]. The workstation hardware specifications used was 2 Nvidia GPUs in parallel configuration, Quadro 4000 with 256 CUDA cores and 2GB VRAM, Quadro M5000 with 2048 CUDA cores and 8GB VRAM, CPU Intel Xeon E5-2687W 32 logical cores 3.1 GHz and 64GB of RAM. All reconstruction algorithms made use of GPU computation. The scan geometry was setup as a 200° arc with 1,000 mm source-isocenter distance, 1,536 mm source-detector distance, full fan 512 × 512 pixel detector with 0.8 × 0.8 mm pixels for adaptive- and conventional-acquisition. Reconstructions were performed using version 2.3.0 of RTK, with hybrid methods not currently natively implemented e.g. MKB, MCMKB and SMEIR assembled using existing functions such as FDK, Simultaneous Algebraic Reconstruction Technique (SART) [22] and Total Variation (TV) [23] denoising using wrappers written in MATLAB. This allowed the optimizations within

each iteration to be computed efficiently with RTK, with the broader iteration steps performed in MATLAB. FDK, MKB, MCMKB and MCFDK images were reconstructed to 270 × 270 × 270 voxels. SMEIR images were reconstructed with an extended field of view and then truncated into 270 x 270 x 270 voxels. Each voxel is 1 mm^3

Reconstruction algorithms

Adaptive- and conventional-acquisition scans were reconstructed with 4DFDK, McKinnon-Bates (MKB) [24], Motion Compensated FDK (MCFDK) [20], Motion Compensated MKB (MCMKB) [9] and Simultaneous Motion Estimation and Image Reconstruction (SMEIR) [8] algorithms. Further details with graphical representation of 4DFDK, MKB, MCFDK and MCMKB implementations used in this study can be found in [25]. Deformable image registration (DIR) for MCFDK, MCMKB and SMEIR was performed using the Elastix Toolkit.

The FDK and MKB methods benefit from rapid image reconstruction that suits patient treatment timeframes. These methods generate images with adequate contrast and sharpness at the cost of imaging time and dose. However, they suffer from motion blur as motion information is not considered. Nevertheless, this has motivated the development of motion compensated strategies namely MCFDK, MCMKB and SMEIR methods which can produce images with improved contrast and sharpness, as well as low motion blur over current clinical implementations. However, each method has its own tradeoffs.

The MCFDK method relies solely on the planning 4DCT, changes in respiratory motion between planning 4DCT and 4DCBCT scan may impact the accuracy of the images. The benefit of the MCFDK method is that the deformable vector fields (DVF)s can be computed before the treatment day, allowing fast image reconstruction.

To address the issues with MCFDK using an the DVF from the planning CT, the MCMKB method was developed to use up-to-date motion models derived from 4DCBCT data. However, the longest step in terms of computation time is the time taken to generate the motion model (DVF) from the MKB reconstruction.

Our current implementation computes the DVF in 10-20 minutes which will need improvements to suit current clinical timeframes. As for improvements, both of the MCFDK and MCMKB methods can benefit from generating a motion model for each phase which could potentially improve the accuracy of tumor and diaphragm motion in the reconstructed images.

There have recently been a number of novel improvements to the SMEIR algorithm. Due to the long computation times and the continued progress in improving the SMEIR algorithm, we chose to implement the original SMEIR algorithm to determine if there is merit in the approach. Specifically, the SMEIR method suffers from limited accuracy in regions with fine details (as DVFs are updated solely on image intensity) and current implementation require long computational times that is not currently suitable for clinical use. Mitigation strategies include SMEIR-Bio [26] which uses biomechanical models to account for physiological behaviours in small structures, G-SMEIR [27] and m-SMEIR [28] which addresses local minima trapping by using image-domain to improve DVF estimation. Additionally, similar iterative methods that exclusively fit to data such as McSART [29] can also provide enhanced motion prediction as it compensates for motion within each reconstructed bin. Overall, these solutions will further improve the small structure detail and motion estimation of SMEIR-*reconstructions,* but again current implementation have long computation times.

Feldkamp-Davis-Kress (FDK)

The current clinical standard for 4DCBCT reconstructions is the 4DFDK algorithm [1]. Adaptive- and conventional-acquisitions were reconstructed using RTK implementation of FDK [21]. To generate FDK reconstructions, a Hann filtering coefficient of 0.9 and sinogram padding of 10 pixels was used to replicate the image quality produced in current commercial clinical systems.

Motion Compensated Feldkamp-Davis Kress (MCFDK)

The MCFDK algorithm accounts for underlying respiratory motion by back projecting along curved paths, whereas the conventional FDK algorithm back projects along straight paths [20]. Motion models were

developed by performing DIR between each 4DCT respiratory phase binned volumes with Elastix Toolkit's B-spline registration [30]. Peak inhale (respiratory phase 6) was used as the reference volume for DIR. DVFs generated from 4DCT DIR are applied to FDK volumes to form the MCFDK volumes. The MCFDK algorithm is the only method in this study that uses prior data, relying on the planning 4DCT to generate the motion models.

McKinnon–Bates (MKB)

The MKB algorithm makes use of 4DFDK volumes and simulated 4DFDK volumes (simulated through the 3DFDK volume) to generate MKB volumes. The motivation of this method is to generate MKB volumes that resemble the low noise of 3DFDK volumes and low motion blur of 4DFDK volumes. The MKB implementation used in this study differs slightly to the original MKB article [24], difference volumes are used rather than difference projections to prevent overflow issues.

Motion compensated McKinnon–Bates (MCMKB)

The MCMKB algorithm back projects along curved paths to account for respiratory motion [9]. DIR is performed between each MKB respiratory binned volumes to generate DVFs, which are applied to the original MKB volumes to produce the final MCMKB volumes.

The only difference between the MCMKB and MCFDK algorithm is the DVF source. The MCFDK algorithm relies on the DVF generated from the planning 4DCT acquisition whereas the MCMKB algorithm relies on the DVF generated from MKB volumes.

Simultaneous Motion Estimation and Image Reconstruction (SMEIR)

As the name suggests, the SMEIR algorithm simultaneously estimates the patient anatomy and motion through an iterative process. For iteration k, SMEIR estimates a volume that minimizes the residual between measured projections and forward projections through the volume warped by the $k-1$ motion estimate, with the restriction that the volumes total variation should be low. A low total variation corresponds to a sparse image gradient which corresponds to images with distinct regions of internally

homogeneous tissue as expected of an actual patient. With the k'th 4D volume estimated, DIR is performed between each frame to build the k'th motion model. We performed the motion compensated total variation regularized anatomy estimation using RTK, and the motion estimation using the Elastix Toolkit's B-spline method. Motion estimation for SMEIR reconstructions was initialised with null volumes and null DVFs. The majority of the motion estimation was resolved in the initial iterations, with the final SMEIR iterations seeing changes in the DVF comparable to the stochastic gradient descent noise.

Mathematical Summary

We include condensed mathematical summaries for each method below. We notate x as a (vectorized) volume, A as the forward projection matrix, F as a filter matrix (e.g. ramp filter), p as the (vectorized) projection images, A_j, F_j, p_j as the quantities limited to just projections at bin j, $x_{\text{method},j}$ as the volume estimated by the subscripted method corresponding to bin j, $W_{r,j}$ as the warping/motion model from bin j to reference bin r, T as the affine registration (in this case from CT to CBCT). We define the total variation as:

$$TV(x) = \sum_{i,j,k} \sqrt{|x(i,j,k) - x(i-1,j,k)| + |x(i,j,k) - x(i,j-1,k)| + |x(i,j,k) - x(i,j,k-1)|}.$$

Table 1: A mathematical summary of the reconstruction algorithms used in this study.

Algorithm	Mathematical Summary	Notes
3DFDK	$x_{3DFDK} = A^T F p = \frac{1}{10}\sum_j^{10} A_j^T F_j p_j$	Standard 3DFDK Equivalent to the average 4DFDK volume
4DFDK	$x_{4DFDK,j} = A_j^T F_j p_j$	Standard 4DFDK, simply a FDK reconstruction limited to the bin j data.
MKB	$p_{s,j} = A_j x_{3DFDK}$ $x_{s,j} = A_j^T F_j p_{s,j}$ $(\hat{a}, \hat{b}) = \min_{a,b}\left\{\left\|a + b x_{s,j} - x_{4DFDK,j}\right\|_2^2\right\}$ $x_{diff,j} = \hat{a} + \hat{b} x_{s,j} - x_{4DFDK,j}$ $x_{MKB,j} = x_{3DFDK} - x_{diff,j}$	MKB is still based on filtered back projection but includes a forward projection to create simulated 4D data, which are also filtered and back projected, and compared to the true 4DFDK volumes to create difference volumes to add to the 3DFDK volume. Note that 3DFDK and 4DFDK require one evaluation of A^T, while MKB requires 2 evaluations of A^T and one of A, effectively tripling computational cost.
MCMKB	$x_{MKB,r} \approx W_{r,j}(x_{MKB,j})$ $x_{MCMKB,r} = \frac{1}{10}\sum_{j=1}^{10} W_{r,j}(x_{MKB,j})$ $x_{MCMKB,j} = W_{j,r}(x_{MCMKB,r})$	Estimates the motion between MKB volumes, then forms MCMKB volume as the average of the warped volumes.

MCFDK	$x_{4DCT,r} \approx W_{r,j}(x_{4DCT,j})$ $x_{3DFDK} \approx T(x_{3DCT})$ $x_{MCFDK,r} = \frac{1}{10}\sum_{j=1}^{10}\left(T(W_{r,j})\right)(x_{4DFDK,j})$ $x_{MCFDK,j} = \left(T(W_{j,r})\right)(x_{MCFDK,r})$	Estimates motion from planning 4DCT, aligns to 3DFDK, forms MCFDK volume as average of warped volumes.
SMEIR	$x_{SMEIR,r}^{k+1} = \min_{X}\left\{\left\|\sum_{j=1}^{10} A_j W_{r,j}^{k}(x_j^k) - p_j\right\|_2^2 + TV(x_r)\right\}$ $x_{SMEIR,j}^{k+1} = W_{j,r}^{k+1}(x_{SMEIR,r}^{k+1})$	Estimates anatomy via motion compensated total variation regularized reconstruction. The updated motion model is then estimated using B-spline DIR. Both steps are performed at each iteration.

Image Quality Metrics

Quantitative performance of each acquisition-reconstruction method was evaluated using Structural Similarity Index (SSIM), Signal-to-Noise Ratio (SNR), Contrast-to-Noise Ratio (CNR), Tissue Interface Sharpness of Diaphragm (TIS-D) and Tissue Interface Sharpness of Tumor (TIS-T) and Center of Mass Trajectory (COMT) image quality metrics, see Table 2. Truncation artifacts were avoided by computing each image quality metric over Regions of Interest (ROI) within the field of view. Further details of these image quality metrics can be found in our previous study [25]. All metrics were averaged across all 10 bins, except TIS-D and TIS-T which were computed at peak inhale bin.

COMT was used to measure difference in diaphragm and tumor motion across all reconstruction methods, compared with conventional-acquisition 4DFDK-reconstruction. To measure the displacement of diaphragm motion, a $5 \times 5 \times l$ voxel sized ROI was positioned at the top of the diaphragm, with $l \approx 20$ being the run length in the direction of superior-to-inferior axis. These voxel value runs are normalized between the values 0 to 1 and sigmoid fitted. Similarly, to measure the displacement of tumor motion a 3D ROI was selected to encapsulate the entire tumor.

ROI voxel values were automatically transformed and windowed to enable fair comparison between image quality metrics. This was performed by denoting $X_{gt}, X_r \in R^N$ with X_{gt} as the ground truth and X_r as the reconstruction voxel value vectors (of size N voxels) and $x_{gt}, \hat{x_r} \in R^n$ represents the ROI ground truth and ROI reconstruction voxel value vectors (of size $n < N$ voxels). Transformed and windowed ROI voxel values are $x_r = \hat{a}\hat{x}_r + \hat{b}$ where $(\hat{a}, \hat{b}) = \min_{a,b} \left\{ \left\| x_{gt} - a x_r - b \right\|_2^2 \right\}$

Table 2: A mathematical summary of the image quality metrics used in this study.

Image Quality Metric	Mathematical Summary	Notes

SSIM	$\frac{(2\mu_{gt}\mu_r + c_1)(2\sigma_{r,gt} + c_2)}{(\mu_{gt}^2 + \mu_r^2 + c_2)(\sigma_{gt}^2 + \sigma_r^2 + c_2)}$	μ and σ^2 represent voxel value means and variances of the ROI, $c_1 = (0.01L)^2$ and $c_2 = (0.03L)^2$ where L is the dynamic range of the volumes. A higher value represents the reconstructed image is similar in image quality compared to conventional-acquisition 4DFDK-reconstruction.
SNR	$\frac{\mu_{Diaphragm}}{\sigma_{Diaphragm}}$	μ represents the voxel value means, whereas σ is the standard deviation of voxel values. A higher value represents more signal than noise.
CNR	$\frac{\lvert\mu_{Diaphragm} - \mu_{Lung}\rvert}{\sigma_{Diaphragm}}$	μ represents the voxel value means, whereas σ is the standard deviation of voxel values. A higher value represents better image contrast.
TIS-D	$f(x,a,c) = \frac{1}{1+e^{-a(x-c)}}$ $(a_j, c_j) = \min_{a,c}\left\{\left\|V_j - f(x,a,c)\right\|_2^2\right\}$ $TIS = \frac{1}{25}\sum_{j=1}^{25} a_j = \mu_c$	Computes a 5 × 5 × *l* ROI at the top of diaphragm, where *l* is a run of pixels in the direction of superior-to-inferior axis. These voxel value runs are normalized between the values 0 to 1 and sigmoid fitted. This measures the sharpness of the edge at the diaphragm. A higher value represents a sharper result.

TIS-T	$$f(x,a,c) = \frac{1}{1+e^{-a(x-c)}}$$ $$(a_j, c_j) = \min_{a,c}\left\{\left\|V_j - f(x,a,c)\right\|_2^2\right\}$$ $$TIS = \frac{1}{25}\sum_{j=1}^{25} a_j = \mu_c$$	Computes a 5 x 5 x *l* ROI at the edge of the tumor, where *l* is a run of pixels in the direction of superior-to-inferior axis (top of tumor) or inferior to superior (bottom of tumor). These voxel value runs are normalized between the values 0 to 1 and sigmoid fitted. This measures the sharpness at the edge of the tumor. A higher value represents a sharper result.
COMT	$$COM(:) = \begin{pmatrix} \sum_{i\in ROI} \frac{x(i)*i}{m} \\ \sum_{j\in ROI} \frac{x(j)*j}{m} \\ \sum_{k\in ROI} \frac{x(k)*k}{m} \end{pmatrix}$$ $$COMT_{method}(:,n) = \left\|COM_{method}(:,n) - COM_{ref}(:,n)\right\|_2$$	Compute the center of mass in a ROI encompassing a structure of interest e.g. the tumor, and reflects how closely the center of mass follows that of a reference volume across each respiratory phase. A lower value indicates the reconstructed image motion is similar to conventional-acquisition 4DFDK-reconstruction.

3. Results

The typical image quality produced with each acquisition and reconstruction method from patient 2 in the coronal viewing plane is displayed in Figure 3. Patient 2 images were selected as the mediastinum was generally within the field of view. The qualitative sharpness and contrast observed in Figure 3, are reflected across all 20 patients. The quantitative results representing all patients are summarized as boxplots, SSIM in Figure 4, CNR and SNR in Figure 5, TIS-D and tumor TIS-T in Figure 6, difference in diaphragm and tumor motion in Figure 7. Table 3 outlines the predicted times for resampled adaptive-acquisition protocol including the average times for adaptive-acquisition from the ADAPT clinical trial.

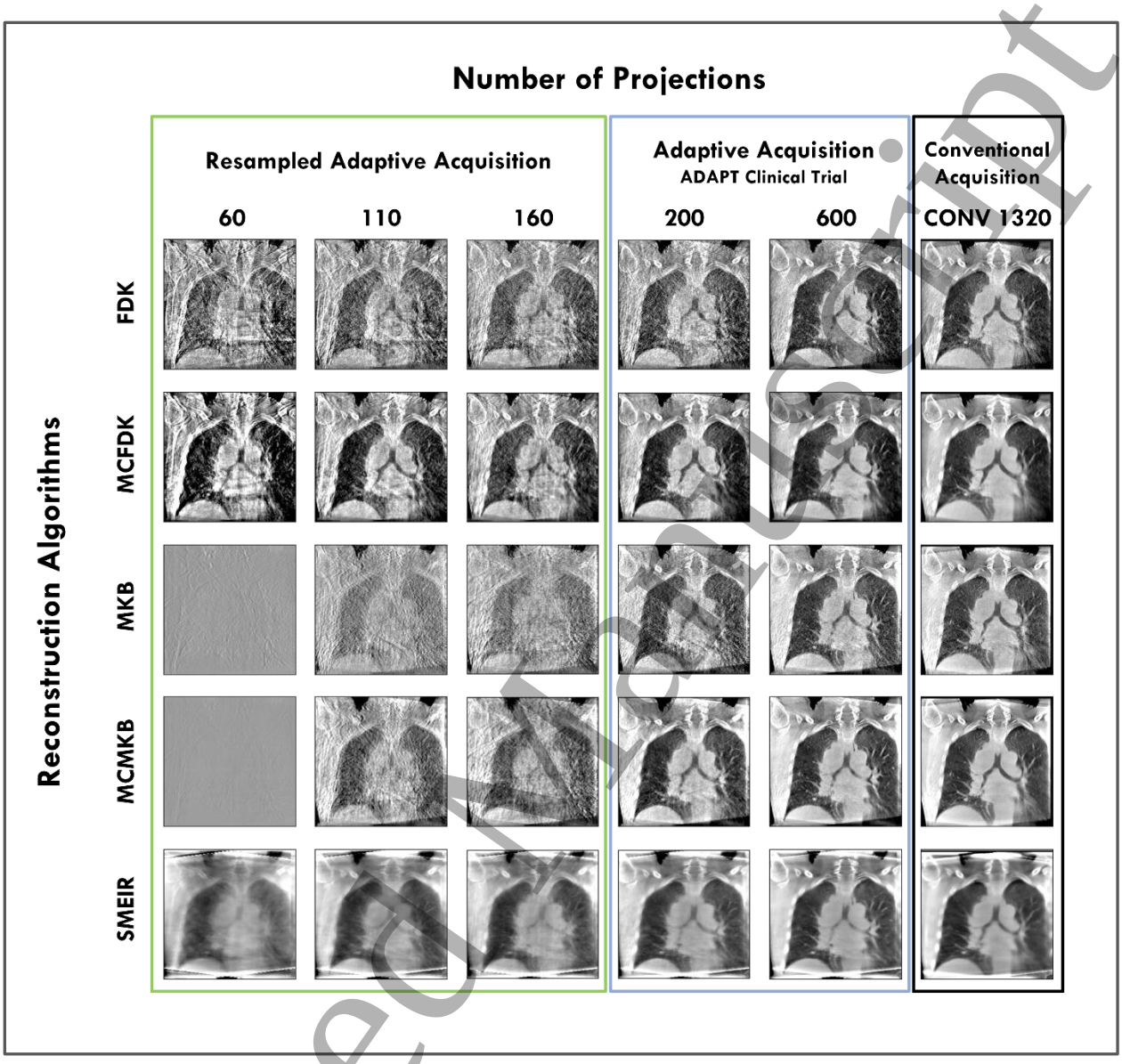

Figure 3: Coronal views of all image reconstruction methods for patient 2. The number above each figure depicts the projection count used for the reconstructions. 60- and 110-projection adaptive-acquisitions were resampled from 200-projection adaptive-acquisitions. 160-projection adaptive-acquisitions were resampled from 600-projection adaptive-acquisitions. Contrast for all images was automatically scaled to conventional-acquisition 4DFDK-reconstruction.

Qualitative Analysis

Overall, visual image quality improves with higher projection count acquisition, irrespective of the reconstruction method. 4DFDK- and MKB-reconstructions (adaptive- and conventional-acquisition), exhibit the highest visual noise and streaking artifacts across all projection counts. Reductions in noise and streaking artifacts were demonstrated through the implementation of motion compensated methods (MCFDK and MCMKB) and motion compensated iterative method (SMEIR).

The SMEIR algorithm maintained relatively consistent image quality as projection count was reduced across all acquisitions with low noise and streaks, however its truncation artifacts were most severe, with regions beyond the ribcage resulting in low contrast. By 60-projections however SMEIR-reconstructions appeared very blurry, obscuring the anatomical features in the mediastinum region.

MCFDK- and MCMKB-reconstructions also produced images with low noise, minimal streak artifacts and enhanced contrast. From 200-projections and above MCFDK- and MCMKB-reconstructions appear visually similar. Below 200-projections, image quality decreased rapidly with MCMKB-reconstruction below 200-projections appearing very noisy and streaky, additionally it was no longer possible to discern anatomical features at 60-projections, a pattern also reflected in MKB-reconstructions. At 60-projection MCFDK-reconstructions, anatomical features were retained, albeit visually streaky and noisy.

MCFDK- and SMEIR-reconstructions were able to maintain visual image quality with as few as 110-projections, comparable to conventional-acquisition 4DFDK-reconstruction.

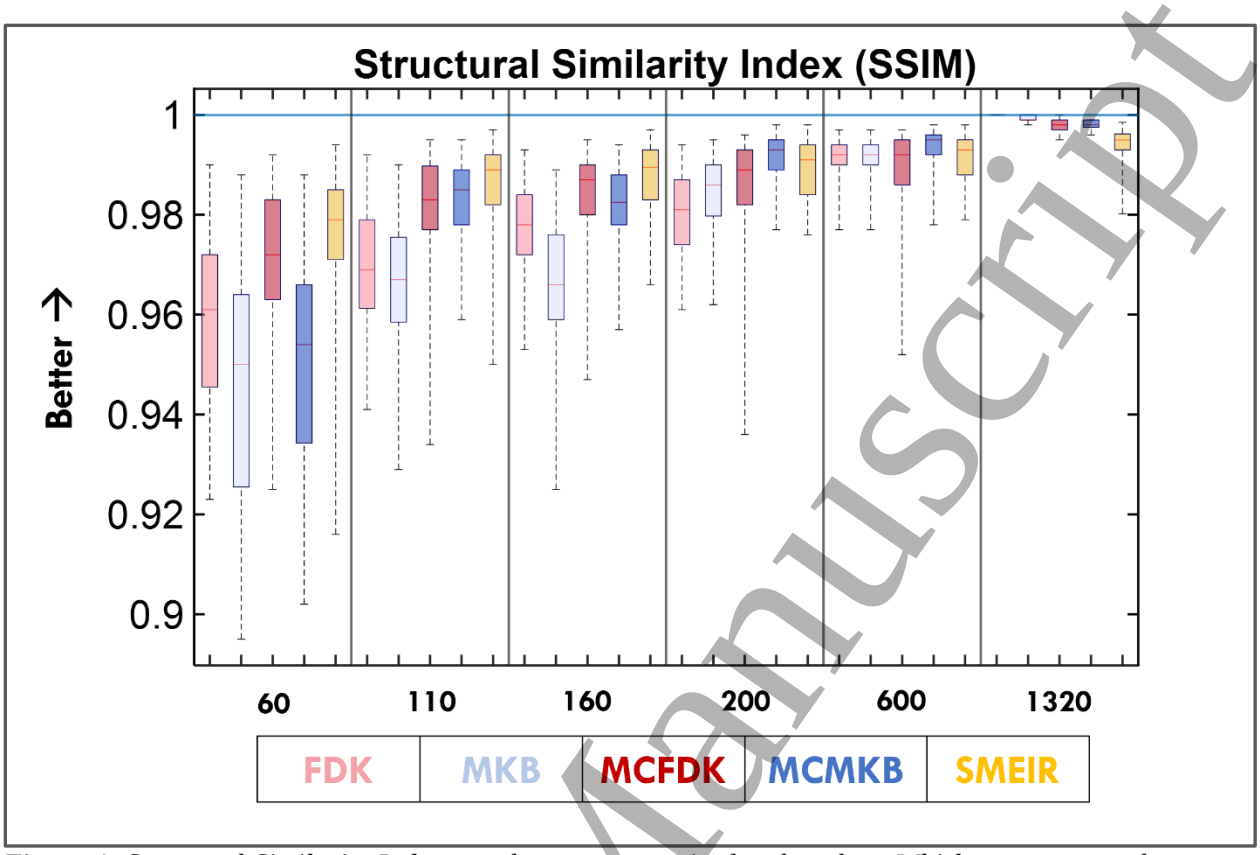

Figure 4: Structural Similarity Index, results are summarized as boxplots. Whiskers represent the range. Each boxplot has been color coded and ordered according to the legend on the bottom. Higher numbers indicate better results. The horizontal line indicates the median value of 1320-projection conventional-acquisition 4DFDK-reconstruction.

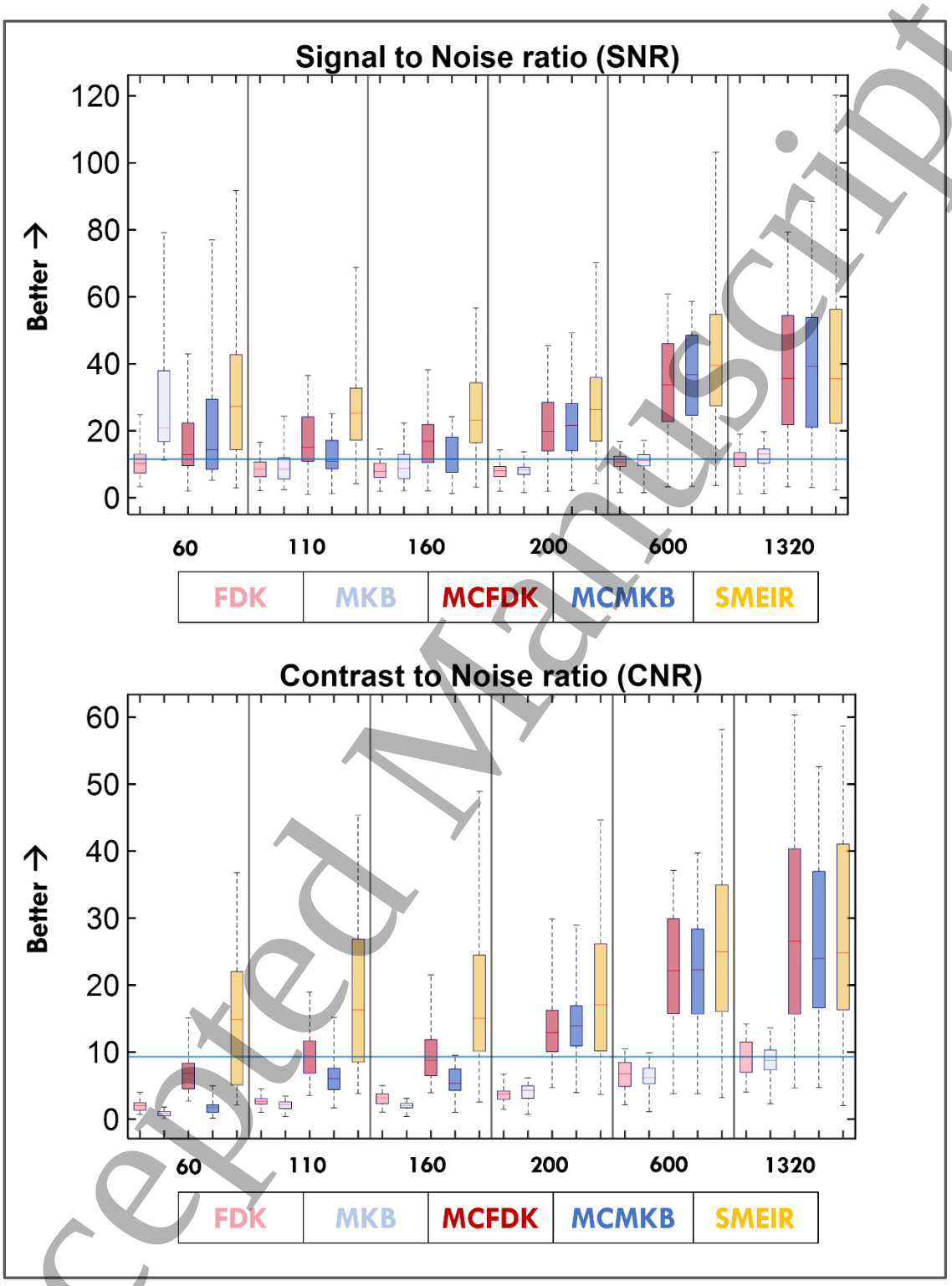

Figure 5: Signal to Noise ratio and Contrast to Noise ratio results are summarized as boxplots. Whiskers represent the range. Each boxplot has been color coded and ordered according to the legend on the bottom. Higher numbers indicate better results. The horizontal line in each boxplot indicates the median value of each metric from the 1320-projection conventional-acquisition 4DFDK-reconstruction.

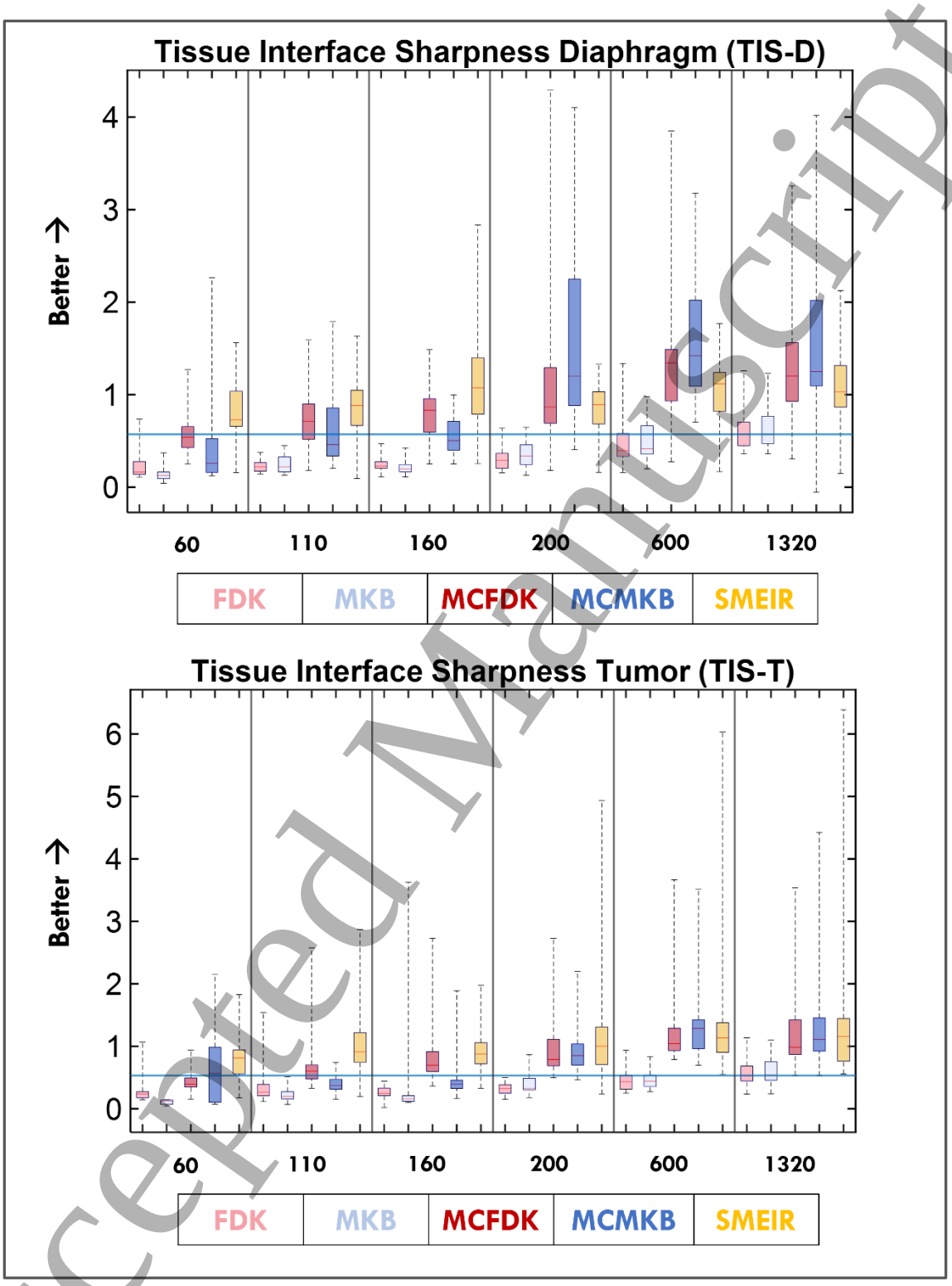

Figure 6: Tissue Interface Sharpness Diaphragm and Tissue Interface Sharpness Tumor results are summarized as boxplots. Whiskers represent the range. Each boxplot has been color coded and ordered according to the legend on the bottom. Higher numbers indicate better results. The horizontal line in each boxplot indicates the median value of each metric from the 1320-projection conventional-acquisition 4DFDK-reconstruction.

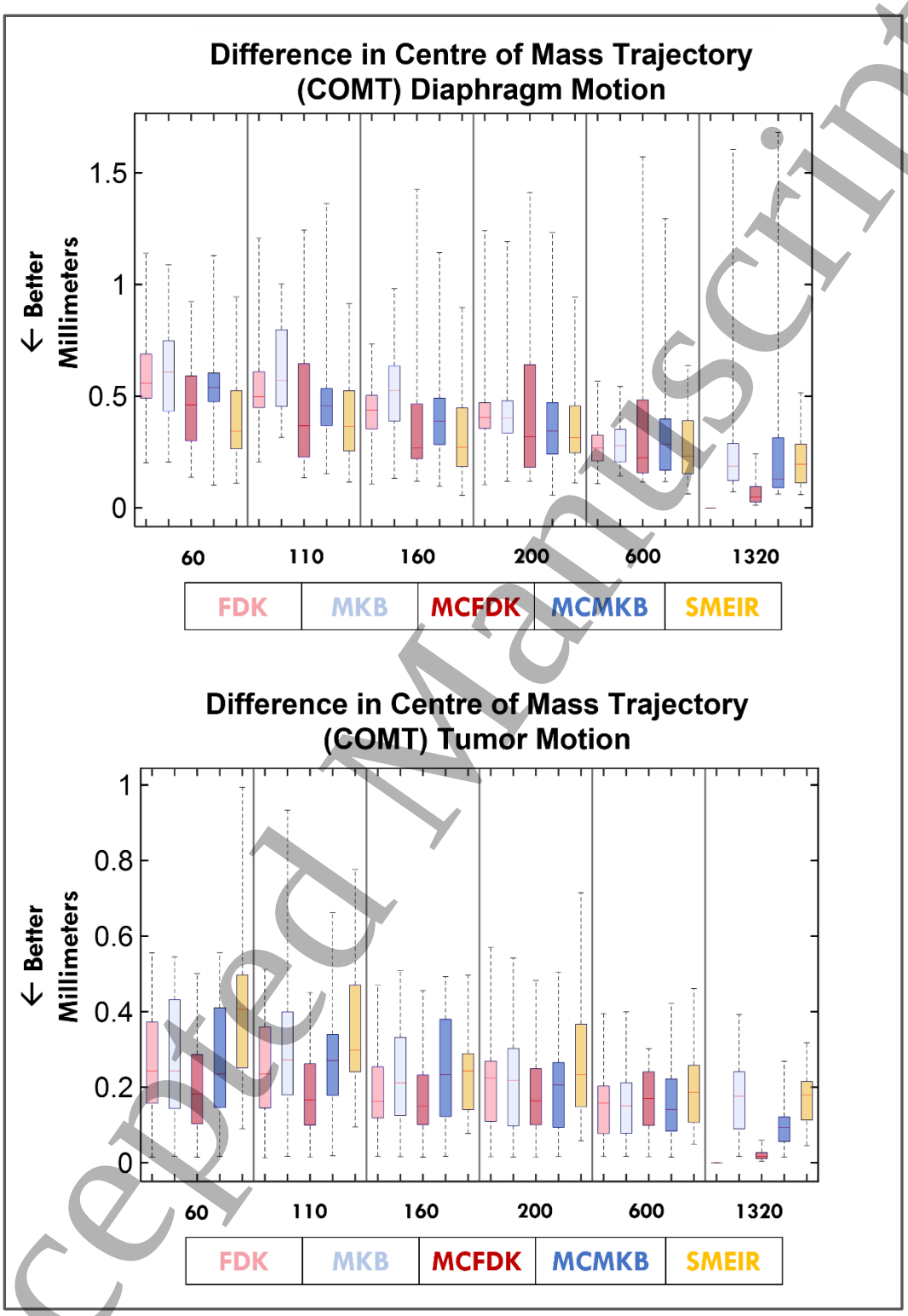

Figure 7: Difference in diaphragm and tumor motion results computed from Centre of Mass Trajectory. Results are phase averaged and summarized as boxplots. Units are in mm and whiskers represent the range. Each boxplot has been color coded and ordered according to the legend on the bottom. Lower values are better, indicating the reconstructed image is closer to the motion of 1320-projection conventional-acquisition 4DFDK-reconstruction.

Table 3: Acquisition time with predicted acquisition time for resampled adaptive-acquisitions. 200- and 600-projection adaptive-acquisitions were acquired from the ADAPT clinical trial, the acquisition time stated in the table were averaged across 2 fractions. Resampled acquisition (60-, 110- and 160-projections) time were approximated based on the number of projections.

	Adaptive Acquisition Time (Seconds)				
Patient Number	**60 Projection (Approximated)**	**110 Projection (Approximated)**	**160 Projection (Approximated)**	**200 Projection (Measured)**	**600 Projection (Measured)**
1	22	41	62	74	232
2	29	52	70	95	264
3	23	42	63	76	237
4	18	33	52	60	195
5	33	60	62	110	234
6	26	47	62	86	232
7	48	89	N/A	161	N/A
8	23	42	67	77	250
9	32	59	88	108	331
10	19	35	43	64	160
11	31	56	36	102	134
12	27	50	86	90	322
13	17	32	46	58	172
14	28	51	74	94	276
15	25	46	72	85	271
16	17	32	45	58	170
17	33	60	69	109	258
18	39	71	91	129	342
19	33	60	73	110	274
20	43	79	89	143	332

Quantitative Analysis

For SSIM, all reconstructions produced high SSIM values comparable to conventional-acquisition 4DFDK-reconstructions (Figure 4). For each reconstruction method, a greater number of projections produced higher SSIM values. Generally FDK- and MKB-reconstructions produced lower SSIM values across all acquisitions. SSIM values improved when motion compensated (MCFDK and MCMKB) and motion compensated iterative (SMEIR) methods were implemented. Below 200 projections MCFDK- and SMEIR-reconstructions yielded the highest SSIM values compared to 4DFDK-reconstructions. While high SSIM can be observed throughout all reconstructions, 60-projection reconstructions suffered the largest drop in SSIM, as well as increased variance.

For SNR and CNR, adaptive-acquisition reconstructions without motion compensation (4DFDK and MKB) performed similar or worse than the conventional-acquisition 4DFDK-reconstructions (Figure 5). Overall at 200-projections and above, motion compensated (MCFDK and MCMKB) and motion compensated iterative (SMEIR) reconstructions performed better than the conventional-acquisition 4DFDK-reconstructions. For reconstructions below 200-projections, 110- and 160-projections MCFDK- and SMEIR-reconstructions produced higher SNR and similar CNR values compared to conventional-acquisition 4DFDK-reconstructions. 110- and 160-projections MCMKB-reconstructions produced similar SNR and lower CNR values compared to the conventional-acquisition 4DFDK-reconstructions. At 60 projections all reconstructions performed worse or similar for CNR than conventional-acquisition 4DFDK-reconstructions. Whilst 60-projection MKB-, MCMKB-, MCFDK- and SMEIR-reconstructions generated higher SNR values than conventional-acquisition 4DFDK-reconstructions, the observed visual image quality was clearly worse, see Figure 3.

Similarly for TIS-D and TIS-T results, reconstructions without motion compensation (4DFDK and MKB) performed similar or worse than conventional-acquisition 4DFDK-reconstrutions (Figure 6). For reconstructions with 200-projections and greater, motion compensated (MCFDK and MCMKB) and motion compensated iterative (SMEIR) reconstructions resulted in higher TIS-D and TIS-T than conventional-acquisition 4DFDK-reconstruction, with SMEIR reconstructions achieving the best results. Below 200-projections, TIS-D and TIS-T performance for MCMKB-reconstructions degraded rapidly, MCFDK-reconstructions also degraded below 200 projections albeit at a slower rate while SMEIR-reconstructions performance remained relatively the same. At 110- and 160-projections both SMEIR- and MCFDK-reconstructions were still able to achieve TIS-D and TIS-T values higher than conventional-acquisition 4DFDK-reconstruction. At 60 projections TIS-D and TIS-T results for MCFDK-, MCMKB- and SMEIR-reconstructions were similar to conventional-acquisition 4DFDK-reconstruction, however the trade-off was lower CNR values and this was evident in the visual appearance of images.

Generally there was wide variation amongst image quality metrics within the MCMKB and SMEIR images, seen in the results as relatively wide plots, specifically for SNR, CNR, and TIS. SNR and CNR involve division by the image intensity variance so for relatively well performing reconstructions the resulting variance in values are large even if absolute differences in variance are small. TIS is an exponential coefficient, so similarly when edges are well defined TIS values can cover a wide range for similar edges.

COMT was used to measure the difference in diaphragm and tumor motion, all acqusition reconstruction methods predominantly achieved submillimeter accuracy compared to conventional- acquisition 4DFDK-reconstruction (Figure 7). In general, reconstructions with more projections resulted in lower deviation from conventional-acquisiton 4DFDK-reconstruction. Motion compensated methods (MCFDK, MCMKB, SMEIR) achieved the closest diaphragm and tumor motion results to conventional-acquisition 4DFDK-reconstruction.

Scan times for 200- and 600-projection adaptive-acquisition were recorded, while adaptive 60-, 110- and 160-projection acquisition times were approximated (Table 3). The scan times are inclusive of any waiting

time if the patient experiences irregular breathing. Conventional-acquisition requires 240 seconds for an acquisition. On average, acqusition times for 200-projection adaptive-acquisitions required 94±27 seconds, and 600-projection adaptive-acqusitions required 246±59 seconds. 60- and 110-projection adaptive-acquisition times were approximated from 200-projection adaptive-acquisitions and averaged 28±8 and 52±15 seconds respectively. While 160-projection adaptive-acquisitions were approximated from 600-projection adaptive-acquisitions and averaged 66±16 seconds respectively.

4. Discussion

The purpose of this study was to investigate the minimum number of projections for adaptive-acquisition to reconstruct images comparable to conventional-acquisition 4DFDK-reconstruction. It is important to note that all data used were acquired as part of 200 and 600 projection adaptive-acquisitions. The limitation of this study is that resampled acquisitions select projections from within the projection sets, but do not correspond to exactly the same evenly spaced projections as a true adaptive-acquisition.

Previous studies showed 200 projections were adequate to reconstruct 4DCBCT images comparable to conventional 4DCBCT when motion compensation was implemented [9, 25]. Here the limits of each reconstruction algorithm were explored, using fewer projections and faster acquisition times.

The results demonstrate 110- and 160-projection adaptive-acquisitions when reconstructed with MCFDK and SMEIR algorithms can further reduce imaging dose and scan time while maintaining image quality, comparable to conventional-acquisition 4DFDK-reconstruction. The COMT for difference in diaphragm and tumor motion for each reconstruction method was generally within submillimeter accuracy in comparison to conventional-acquisition 4DFDK-reconstruction. Moreover, variations in the difference in diaphragm and tumor motion may be caused by intrafraction variations between the conventional-acquisition and adaptive-acquisitions.

We have used the current clinical standard of care conventional 4DFDK as the ground truth for this study. We note that conventional 4DFDK does contain errors and artefacts which may affect comparisons. However, since there is no actual ground truth for this study, performance can only be judged by the current clinical standard. A potential method to improve conventional 4DFDK would be to utilize a longer scan time whilst reducing the imaging frame rate to lower imaging dose. Reducing the frame rate may result in missing respiratory bins for faster breathing patients. Nevertheless, conventional 4DFDK is high projection count which is considered to have very few artefacts and clinically acceptable.

The image quality metrics show that 110- and 160-projection acquisitions reconstructed with MCFDK and the SMEIR algorithms provided better SSIM, SNR, CNR, TIS-D and TIS-T compared to the conventional-acquisition with 4DFDK-reconstructions. These results are reflective of the qualitative analysis of both 110- and 160-projection adaptive-acquisitions against conventional-acquisition 4DFDK-reconstructions. However, 110- and 160-projection adaptive-acquisition MCMKB-reconstructions produced SSIM, SNR, CNR, TIS-D and TIS-T results worse than conventional-acquisition 4DFDK-reconstructions. This was evident in the qualitative results of MCMKB-reconstructions, as acquisitions below 200-projections suffered greatly from streaking and noise artifacts. A possible reason for this occurrence is that MKB-reconstructions become very streaky and noisy below 200-projections, the consequence is inability to produce convergent DVF estimates for MCMKB-reconstructions.

Part of the purpose of this study was to evaluate how few projections were needed before the artefacts, and in turn DVF estimation accuracy, became unacceptable when using adaptive acquisition and motion compensated reconstruction. Rather than evaluating the DVF accuracy directly, the DVF accuracy was measured implicitly by evaluating quality of the final reconstruction images. In this way, “unacceptable” DVF quality would be seen as image quality below current standard conventional acquisition 4DFDK reconstruction images particularly in regard to edge sharpness (the TIS values).

Interestingly the TIS-D and TIS-T performance of SMEIR-reconstructions saturate from 160-projections and above, which could be due to the nature of automatic parameter tuning. Additionally, of all the reconstruction methods, only the MCFDK algorithm provided reasonable image quality at 60-projection acquisition however it was visually noisy and SSIM, SNR, CNR, TIS-D and TIS-T results indicated it was clearly inadequate compared to the conventional-acquisition 4DFDK-reconstruction.

The filtered back projection based methods in this study (except MCMKB) all have computation times comparable to current clinical reconstruction methods while the iterative method (SMEIR) has a reconstruction time that still needs to be reduced for practical clinical implementation.

The current clinical implementation of 4DFDK-reconstruction occurs concurrently with acquisition. The significance is that FDK-reconstructions are accessible moments after acquisition. If the DVFs can be generated offline for MCFDK-reconstructions prior to patient treatment, the computational time is similar to FDK-reconstructions, and therefore reconstruction times are short enough for clinical use. However, the MCFDK algorithm is prior data driven relying on planning 4DCT for motion estimation, so there is a chance this does not reflect the patient's motion on the day of treatment.

In contrast, the MCMKB algorithm computes motion only from data acquired from the 4DCBCT. The drawback for the MCMKB algorithm is the computation time with the slowest process being the computation of the MKB volumes and DVFs requiring approximately 20 minutes in our implementation where our unoptimized implementation computes each respiratory phase in series.

Likewise, SMEIR also uses only data from the 4DCBCT, and has the same draw back regarding computational time. Our implementation of SMEIR required approximately 1.5 hours to compute, currently the slowest step is computing multiple iterations for parameter tuning. Successful clinical implementation of the MCMKB or SMEIR algorithm will require rapid reconstruction and the availability of images prior to treatment. Modern hardware upgrades and software optimization may enable MCMKB and SMEIR algorithms to be viable for clinical applications.

From a clinical standpoint, 110- and 160-projection adaptive acquisitions translate to a reduction of more than 3 minutes on the treatment couch. This shorter time will reduce patient discomfort and reduce patient movement before and during treatment. Reducing imaging dose is instrumental to aligning with the As Low As Reasonably Achievable (ALARA) principle. Furthermore, improvements to image sharpness and contrast could potentially be leveraged to assist hypofractionated treatments of tumors within, or close to, the mediastinum where the tumor is located near radiosensitive organs.

A possible reason why the 60-projection MKB based methods performed poorly is because while the final volumes make use of all projections, intermediate steps involve volumetric reconstructions from just 6

projections. This is in contrast to the MCFDK- and SMEIR-methods which use all available projections in the reconstruction of each volume.

All predicted adaptive-acquisition times are achievable on faster rotating systems such as the Varian Halcyon [31], Accuray Radixact [32], Elekta Versa HD [33]. These current generation linear accelerators are capable of acquiring thoracic scans as fast as 18 – 22 degrees per second, for example this would satisfy a 60-projection adaptive-acquisition as it requires approximately 6 - 10 degrees per second (based on predicted acquisition time of 28±8 seconds). However currently there is no clinical implementation of adaptive-acquisition on the Varian Halcyon, the possibility of a 60-projection adaptive-acquisition will need to be verified in future studies.

Overall, the results suggest each motion compensated method has its own use case for adaptive acquisitions. The SMEIR reconstruction method demonstrated consistently good performance, generating visually similar images across nearly all acquisitions, but suffered from severe truncation artifacts and did not perform as well as the other motion compensated methods above 200-projections. MCMKB-reconstructions offered the sharpest images with high contrast for acquisitions with 200-projections and above but struggled with noise and streaks below 200-projections. MCFDK-reconstructions offered the sharpest images with high contrast below 200-projections, and in contrast to SMEIR- and MCMKB-methods can be performed in a clinically viable time frame. No methods performed well at 60 projections suggesting adaptive acquisition protocols have a lower limit of 110 projections with current reconstruction methods.

5. Conclusion

For the first time, this study examined reductions in computation time and imaging dose using a combination of resampled adaptive-acquisition and emerging motion compensated image reconstruction techniques. Our findings demonstrate imaging times and dose can be substantially reduced, whilst

maintaining image quality comparable to conventional-acquisition 4DFDK-reconstruction implemented in the clinic.

6. Acknowledgements

We would like to acknowledge the patients who participated in the ADAPT trial, offering their time and imaging dose. This study was funded by NHMRC grant 1138899 and partly by a Cancer Australia (Priority-driven Collaborative Cancer Research Scheme) project grant number 1123068. Paul Keall is supported by an Australian NHMRC Leadership Fellowship. We thank Dr Helen Ball, Dr Mark Gardner and Dr Mir Massoud Aghili Yajadda for critical review of the manuscript, and Julia Johnson in assisting with figures. We thank Elekta for allowing us to implement ADAPT technology on their linear accelerator for the ADAPT clinical trial. We wish to also thank the staff of the Department of Radiation Oncology at Liverpool Hospital for their contributions to this study. Ricky O'Brien and Paul Keall are inventors on a patent underpinning the adaptive imaging technology in this paper.

7. References

1. J.J. Sonke, L. Zijp, P. Remeijer, and M. van Herk, "Respiratory correlated cone beam CT", *Medical physics*, vol. 32, no. 4, pp. 1176-1186, 2005

2. H. Gao, R. Li, Y. Lin, and L. Xing, "4D cone beam CT via spatiotemporal tensor framelet", *Medical physics*, vol. 39, no. 11, pp. 6943-6946, 2012

3. T. Li, A. Koong, and L. Xing, "Enhanced 4D cone‐beam CT with inter‐phase motion model", *Medical physics*, vol. 34, no. 9, pp. 3688-3695, 2007

4. T. Li and L. Xing, "Optimizing 4D cone-beam CT acquisition protocol for external beam radiotherapy", *International Journal of Radiation Oncology Biology Physics*, vol. 67, no. 4, pp. 1211-1219, 2007

5. J. Lu, T.M. Guerrero, P. Munro, A. Jeung, P.C.M. Chi, P. Balter, X.R. Zhu, R. Mohan, and T. Pan, "Four‐dimensional cone beam CT with adaptive gantry rotation and adaptive data sampling", *Medical physics*, vol. 34, no. 9, pp. 3520-3529, 2007

6. J. Bian, J.H. Siewerdsen, X. Han, E.Y. Sidky, J.L. Prince, C.A. Pelizzari, and X. Pan, "Evaluation of sparse-view reconstruction from flat-panel-detector cone-beam CT", *Physics in Medicine & Biology*, vol. 55, no. 22, pp. 6575-6599, 2010

7. R.T. O'Brien, J. Kipritidis, C.-C. Shieh, and P.J. Keall, "Optimizing 4DCBCT projection allocation to respiratory bins", *Physics in Medicine & Biology*, vol. 59, no. 19, pp. 5631, 2014

8. J. Wang and X. Gu, "Simultaneous motion estimation and image reconstruction (SMEIR) for 4D cone‐beam CT", *Medical physics*, vol. 40, no. 10, pp. 101912, 2013

9. O. Dillon, P.J. Keall, C.-C. Shieh, and R. O'Brien, "Evaluating reconstruction algorithms for respiratory motion guided acquisition", *Physics in Medicine & Biology*, vol. 65, no. 17, 2020

10. R.T. O'Brien, O. Dillon, B. Lau, A. George, S. Smith, A. Wallis, J.-J. Sonke, P.J. Keall, and S.K. Vinod, "The first-in-human implementation of adaptive 4D cone beam CT for lung cancer radiotherapy: 4DCBCT in less time with less dose", *Radiotherapy and Oncology*, vol. no., 2021

11. M.F. Fast, E. Wisotzky, U. Oelfke, and S. Nill, "Actively triggered 4d cone‐beam CT acquisition", *Medical physics*, vol. 40, no. 9, pp. 091909, 2013

12. B.J. Cooper, R.T. O'Brien, and P.J. Keall, "Respiratory Signal Triggered 4D Cone‐Beam Computed Tomography on a Linear Accelerator", *Medical Physics*, vol. 39, no. 6Part2, pp. 3605-3605, 2012

13. R.T. O'Brien, B.J. Cooper, C.-C. Shieh, U. Stankovic, P.J. Keall, and J.J. Sonke, "The first implementation of respiratory triggered 4DCBCT on a linear accelerator", *Physics in Medicine & Biology*, vol. 61, no. 9, pp. 3488, 2016

14. B.J. Cooper, R.T. O'Brien, S. Balik, G.D. Hugo, and P.J. Keall, "Respiratory triggered 4D cone‐beam computed tomography: A novel method to reduce imaging dose", *Medical physics*, vol. 40, no. 4, 2013

15. B.J. Cooper, R. O'Brien, J. Kipritidis, C.-C. Shieh, and P.J. Keall, "Quantifying the image quality and dose reduction of respiratory triggered 4D cone-beam computed tomography with patient-measured breathing", *Physics in Medicine & Biology*, vol. 60, no. 24, pp. 9493, 2015

16. R.T. O'Brien, B.J. Cooper, and P.J. Keall, "Optimizing 4D cone beam computed tomography acquisition by varying the gantry velocity and projection time interval", *Physics in Medicine & Biology*, vol. 58, no. 6, pp. 1705, 2013

17. R.T. O'Brien, B.J. Cooper, J. Kipritidis, C.-C. Shieh, and P.J. Keall, "Respiratory motion guided four dimensional cone beam computed tomography: encompassing irregular breathing", *Physics in Medicine & Biology*, vol. 59, no. 3, pp. 579, 2014

18. R.T. O'Brien, U. Stankovic, J.J. Sonke, and P.J. Keall, "Reducing 4DCBCT imaging time and dose: the first implementation of variable gantry speed 4DCBCT on a linear accelerator", *Physics in Medicine & Biology*, vol. 62, no. 11, pp. 4300, 2017

19. R.T. O'Brien, U. Stankovic, P. Keall, and J.J. Sonke, "Respiratory Motion Guided 4DCBCT‐A Step Towards Controlling 4DCBCT Image Quality", *Medical physics*, vol. 43, no. 6, pp. 3800-3800, 2016

20. S. Rit, J.W. Wolthaus, M. van Herk, and J.J. Sonke, "On‐the‐fly motion‐compensated cone‐beam CT using an a priori model of the respiratory motion", *Medical physics*, vol. 36, no. 6, pp. 2283-2296, 2009

21. S. Rit, M.V. Oliva, S. Brousmiche, R. Labarbe, D. Sarrut, and G.C. Sharp. *The Reconstruction Toolkit (RTK), an open-source cone-beam CT reconstruction toolkit based on the Insight Toolkit (ITK)*. in *J Phys Conf Ser*. 2014.

22. A.H. Andersen and A.C. Kak, "Simultaneous algebraic reconstruction technique (SART): a superior implementation of the ART algorithm", *Ultrasonic imaging*, vol. 6, no. 1, pp. 81-94, 1984

23. A. Chambolle, "An algorithm for total variation minimization and applications", *Journal of Mathematical imaging and vision*, vol. 20, no. 1, pp. 89-97, 2004

24. G.C. Mc Kinnon and R. Bates, "Towards imaging the beating heart usefully with a conventional CT scanner", *IEEE Transactions on Biomedical Engineering*, vol. no. 2, pp. 123-127, 1981

25. B.K. Lau, T. Reynolds, A. Wallis, S. Smith, A. George, P.J. Keall, J.-J. Sonke, S.K. Vinod, O. Dillon, and R. T O'Brien, "Reducing 4DCBCT scan time and dose through motion compensated acquisition and reconstruction", *Physics in Medicine & Biology*, vol. 66, no. 7, pp. 075002, 2021

26. X. Huang, Y. Zhang, and J. Wang, "A biomechanical modeling-guided simultaneous motion estimation and image reconstruction technique (SMEIR-Bio) for 4D-CBCT reconstruction", *Physics in Medicine & Biology*, vol. 63, no. 4, pp. 045002, 2018

27. S. Zhou, Y. Chi, J. Wang, and M. Jin, "General simultaneous motion estimation and image reconstruction (G-SMEIR)", *Biomedical Physics & Engineering Express*, vol. 7, no. 5, pp. 055011, 2021

28. C. Zhao, Y. Zhong, J. Wang, and M. Jin. *Modified simultaneous motion estimation and image reconstruction (m-SMEIR) for 4D-CBCT*. in *2018 IEEE 15th International Symposium on Biomedical Imaging (ISBI 2018)*. 2018. IEEE.

29. G. Chee, D. O'Connell, Y. Yang, K. Singhrao, D. Low, and J. Lewis, "McSART: an iterative model-based, motion-compensated SART algorithm for CBCT reconstruction", *Physics in Medicine & Biology*, vol. 64, no. 9, pp. 095013, 2019

30. S. Klein, M. Staring, K. Murphy, M.A. Viergever, and J.P. Pluim, "Elastix: a toolbox for intensity-based medical image registration", *IEEE transactions on medical imaging*, vol. 29, no. 1, pp. 196-205, 2009

31. B. Cai, E. Laugeman, T.R. Mazur, J.C. Park, L.E. Henke, H. Kim, G.D. Hugo, S. Mutic, and H. Li, "Characterization of a prototype rapid kilovoltage x‐ray image guidance system designed for a ring shape radiation therapy unit", *Medical physics*, vol. 46, no. 3, pp. 1355-1370, 2019

32. K. Kraus, S. Kampfer, J. Wilkens, L. Schüttrumpf, and S. Combs, "Helical tomotherapy: Comparison of Hi-ART and Radixact clinical patient treatments at the Technical University of Munich", *Scientific reports*, vol. 10, no. 1, pp. 1-10, 2020

33. A. Arns, H. Wertz, J. Boda-Heggemann, F. Schneider, M. Blessing, Y. Abo-Madyan, V. Steil, F. Wenz, and J. Fleckenstein, "Ultrafast single breath-hold cone-beam CT lung cancer imaging with faster linac gantry rotation", *Radiotherapy and Oncology*, vol. 135, no., pp. 78-85, 2019